





Radio Observations of an Ordinary Outflow from the Tidal Disruption Event AT2019dsgY. CENDES ¹, K. D. ALEXANDER ^{2,*}, E. BERGER¹, T. EFTEKHARI¹, P. K. G. WILLIAMS ^{1,3} AND
R. CHORNOCK ²¹*Center for Astrophysics / Harvard & Smithsonian, Cambridge, MA 02138, USA*²*Center for Interdisciplinary Exploration and Research in Astrophysics (CIERA) and Department of Physics and Astronomy,
Northwestern University, Evanston, IL 60208, USA*³*American Astronomical Society, 1667 K Street NW, Suite 800 Washington, DC 20006 USA***ABSTRACT**

We present detailed radio observations of the tidal disruption event (TDE) AT2019dsg, obtained with the Very Large Array (VLA) and the Atacama Large Millimeter/submillimeter Array (ALMA), and spanning 55–560 days post-disruption. We find that the peak brightness of the radio emission increases until ~ 200 days and subsequently begins to decrease steadily. Using the standard equipartition analysis, including the effects of synchrotron cooling as determined by the joint VLA-ALMA spectral energy distributions, we find that the outflow powering the radio emission is in roughly free expansion with a velocity of $\approx 0.07c$, while its kinetic energy increases by a factor of about 5 from 55 to 200 days and plateaus at $\approx 4.4 \times 10^{48}$ erg thereafter. The ambient density traced by the outflow declines as $\approx R^{-1.7}$ on a scale of $\approx (1 - 4) \times 10^{16}$ cm ($\approx 6300 - 25000 R_s$), followed by a steeper decline to $\approx 7 \times 10^{16}$ cm ($\approx 44000 R_s$). Allowing for a collimated geometry, we find that to reach even mildly relativistic velocities ($\Gamma = 2$) the outflow requires an opening angle of $\theta_j \approx 2^\circ$, which is narrow even by the standards of GRB jets; a truly relativistic outflow requires an unphysically narrow jet. The outflow velocity and kinetic energy in AT2019dsg are typical of previous non-relativistic TDEs, and comparable to those from Type Ib/c supernovae, raising doubts about the claimed association with a high-energy neutrino event.

Keywords: black hole physics**1. INTRODUCTION**

A tidal disruption event (TDE) occurs when a star wanders sufficiently close to a supermassive black hole (SMBH) to be torn apart by tidal forces. In recent years, the number of observed TDEs has increased dramatically, primarily thanks to wide-field optical time-domain surveys¹. So far, only about 10 TDEs (about 10% of the known sample) have been detected in the radio during dedicated follow-up observations (see Table 1; [Alexander et al. 2020](#)). Even within this small sample it appears that TDEs launch either non-relativistic outflows ($v \sim 0.1c$) with an energy scale of $E_K \sim 10^{48} - 10^{49}$ erg (e.g., [Alexander et al. 2016](#)), or much more rarely relativistic outflows as observed in Swift J1644+57 with

$\Gamma \sim \text{few}$ and $E_K \sim 10^{52}$ erg (e.g., [Zauderer et al. 2011](#); [Berger et al. 2012](#)). The origin of the outflowing material, its relation to the overall TDE properties, and the physical distinction between events that launch relativistic jets and non-relativistic outflows remain a matter of debate.

The TDE AT2019dsg ($z = 0.051$) was discovered by the Zwicky Transient Facility (ZTF) on 2019 April 9, and classified as a TDE based on its optical spectrum. Its peak optical luminosity ($\sim 10^{44.5}$ erg s⁻¹) places it in the top 10% of optical TDEs to date ([van Velzen et al. 2020](#)), and a high level of optical polarization was observed at early times ([Lee et al. 2020](#)). AT2019dsg also exhibited X-ray emission and radio emission in the first few months following discovery ([Cannizzaro et al. 2020](#); [Stein et al. 2021](#)). Additionally, [Stein et al. \(2021\)](#) claim a potential coincident high-energy neutrino with the spatial location of AT2019dsg, but several months after discovery (on 2019 October 1); the emission mechanism for such a neutrino is debated ([Fang et al. 2020](#);

Corresponding author: Yvette Cendes
yvette.cendes@cfa.harvard.edu

* NHFP Einstein Fellow

¹ See <http://tde.space>.

Winter & Lunardini 2020; Liu et al. 2020; Murase et al. 2020).

Here, we present multi-frequency radio observations of AT 2019dsg on a timescale of about 55 to 560 days post disruption, which we use to infer the time evolution of the TDE outflow’s energy and velocity, as well as the circumnuclear medium density profile. In §2, we present our observations using both the Karl G. Jansky Very Large Array (VLA) and the Atacama Large Millimeter/submillimeter Array (ALMA). In §3 we model the individual radio spectral energy distributions (SEDs) and carry out an equipartition analysis to determine the physical properties of the outflow and the ambient medium. In §4 we discuss our findings in the context of the TDE population. We summarize our conclusions in §5.

2. OBSERVATIONS

We obtained radio observations of AT 2019dsg with the VLA spanning from L- to K-band (1–26.5 GHz; Program IDs: 19A-013 and 20A-372; PI: Alexander). The data are summarized in Table 1. We processed the data using standard data reduction procedures in the Common Astronomy Software Application package (CASA; McMullin et al. 2007) accessed through the python-based `pwkit` package² (Williams et al. 2017). We performed bandpass and flux density calibration using either 3C286 or 3C147 as the primary calibrator for all observations and frequencies. We used J2035+1056 as the phase calibrator for L and S bands and J2049+1003 as the phase calibrator for all other frequencies. We imaged the data using the CASA task CLEAN, splitting the data into subbands by frequency when the target was sufficiently bright. We obtained all flux densities and uncertainties using the `imtool fitsrc` command within `pwkit`. We assumed a point source fit, as preferred by the data.

We also observed AT 2019dsg with ALMA in band 3 (mean frequency of 97.5 GHz) on 2019 June 22 and September 17 (Table 1). For the ALMA observations, we used the standard NRAO pipeline to calibrate and image the data. The source was not bright enough for self-calibration. We detect AT 2019dsg in the June observation and derive an upper limit in the September observation (Table 1).

Table 1. VLA and ALMA Observations of AT 2019dsg

Date (UTC)	δt (d)	Array Con- figuration	ν (GHz)	F_ν (mJy)
2019 May 24	55	B	5	0.09 ± 0.01
			7	0.19 ± 0.01
			13	0.48 ± 0.02
			15	0.54 ± 0.02
			17	0.58 ± 0.02
2019 May 29	60	B	3.4	0.77 ± 0.03
			9	0.43 ± 0.03
			11	0.51 ± 0.02
			13	0.63 ± 0.04
			15	0.61 ± 0.03
			17	0.68 ± 0.03
			19	0.73 ± 0.04
			21	0.71 ± 0.05
			23	0.67 ± 0.04
			25	0.59 ± 0.04
			30	0.59 ± 0.04
			32	0.48 ± 0.04
2019 June 20	82	B	34	0.51 ± 0.08
			36	0.46 ± 0.05
			5	0.26 ± 0.02
			7	0.49 ± 0.02
			9	0.68 ± 0.02
			11	0.72 ± 0.03
			13	0.75 ± 0.02
			15	0.65 ± 0.03
			17	0.63 ± 0.02
			19	0.51 ± 0.03
2019 June 22	84	C43-9/10	21	0.46 ± 0.04
			23	0.43 ± 0.05
			25	0.40 ± 0.03
			30	0.33 ± 0.04
			32	0.27 ± 0.03
			34	0.31 ± 0.03
			36	0.24 ± 0.04
			97.5	0.07 ± 0.01
2019 Sept 7	161	A	2.6	0.29 ± 0.03
			3.4	0.42 ± 0.03
			5	0.56 ± 0.02
			7	0.89 ± 0.02
			9	1.03 ± 0.03

² <https://github.com/pkgw/pwkit>

Table 1 *continued*

Table 1 (*continued*)

Date (UTC)	δt (d)	Array Con- figuration	ν (GHz)	F_ν (mJy)
			11	1.08 ± 0.05
			13	1.02 ± 0.02
			15	0.91 ± 0.02
			17	0.80 ± 0.04
			19	0.70 ± 0.04
			21	0.62 ± 0.05
			23	0.58 ± 0.06
			25	0.41 ± 0.05
2019 Sept 17	188	C43-6	97.5	< 0.09
2020 Jan 24	300	D	2.6	0.67 ± 0.04
			3.4	0.82 ± 0.03
			5	0.79 ± 0.03
			7	0.68 ± 0.03
			9	0.46 ± 0.03
			11	0.48 ± 0.45
			13	0.31 ± 0.02
			15	0.27 ± 0.02
			17	0.23 ± 0.03
2020 Oct 11	561	B	1.5	0.35 ± 0.05
			2.6	0.26 ± 0.02
			3.4	0.17 ± 0.01
			6.0	0.13 ± 0.01

NOTE—Errors are statistical only. Upper limits are 3σ .

3. MODELING AND ANALYSIS

To roughly determine the time that the radio-emitting outflow was launched, we fit a second-order polynomial to the first 5 optical r -band flux measurements, which capture the rising part of the light curve (see Table S6; Stein et al. 2021) in order to estimate the time of zero optical flux as a proxy for the time of disruption. We find a date of 2019 March 30 (MJD 58572.8; about 10 days before optical discovery), which we use in Table 1 and in our subsequent analysis. With this choice we find that the outflow is roughly in free expansion (§3.4), validating our approach.

3.1. Modeling of the Radio Spectral Energy Distributions

The individual radio SEDs are shown in Figure 1, where we have also included for completeness³, and therefore do not incorporate the e-MERLIN data in our SEDs. the data presented in Stein et al. (2021). The SEDs are characteristic of self-absorbed synchrotron emission, with a well defined peak frequency (ν_p) and flux density ($F_{\nu,p}$), and a spectral shape of $F_\nu \approx \nu^{5/2}$ below ν_p .

We fit the SEDs⁴ with the model developed by Granot & Sari (2002) for synchrotron emission from gamma-ray burst (GRB) afterglows, specifically in the regime where $\nu_m \ll \nu_a$; this is relevant for non-relativistic sources as validated by the analysis below. We have chosen the stellar wind (k=2) solutions from Granot & Sari (2002) as the closest approximation to the expected circumnuclear density profile surrounding the TDE SMBH. The model SED is given by:

$$F_\nu = F_\nu(\nu_m) \left[\left(\frac{\nu}{\nu_m} \right)^2 e^{-s_4(\nu/\nu_m)^{2/3}} + \left(\frac{\nu}{\nu_m} \right)^{5/2} \right] \times \left[1 + \left(\frac{\nu}{\nu_a} \right)^{s_2(\beta_2 - \beta_3)} \right]^{-1/s_2}, \quad (1)$$

where $\beta_2 = 5/2$, $\beta_3 = (1 - p)/2$, $s_4 = 3.63p - 1.60$, and $s_2 = 1.25 - 0.18p$. Here, p is the electron energy distribution power law index — $N(\gamma_e) \propto \gamma_e^{-p}$ for $\gamma_e \geq \gamma_m$ — ν_m is the frequency corresponding to γ_m , ν_a is the synchrotron self-absorption frequency, and $F_\nu(\nu_m)$ is the flux normalization at $\nu = \nu_m$.

We determine the best fit parameters using the Python Markov Chain Monte Carlo (MCMC) module `emcee` (Foreman-Mackey et al. 2013), assuming a Gaussian likelihood for the parameters $F_\nu(\nu_m)$ and ν_a . Since $\nu_m \ll \nu_a$ we set its value below the range of our data ($\nu_m = 0.1$ GHz). In an initial round of modeling, we first fit for p as a free parameter in each epoch (with a uniform prior of $p = 2 - 4$). We then exclude the epochs where the resulting uncertainty on p is $\delta p \geq 0.2p$, which is due to the paucity of data at $\gtrsim \nu_a$ (e.g., SEDs at days 52, 55). We find no evidence for a time evolution in the value of p , with a weighted average of $p = 2.7 \pm 0.2$, which we adopt in our subsequent analysis. We also

³ We compared our VLA data to the e-MERLIN observations at 5.1 GHz, some of which overlap with our observations (Cannizzaro et al. 2020). The September 7 e-MERLIN flux densities appear systematically higher than our own. After further investigation, we conclude that this is due to differences in the data processing technique.

⁴ For the SEDs at days 130 and 161 we exclude from the modeling the data at 1 – 3 GHz that clearly deviate from the expected spectral shape (open points in Figure 1). We attribute these fluctuations to interstellar scintillation (§ A).

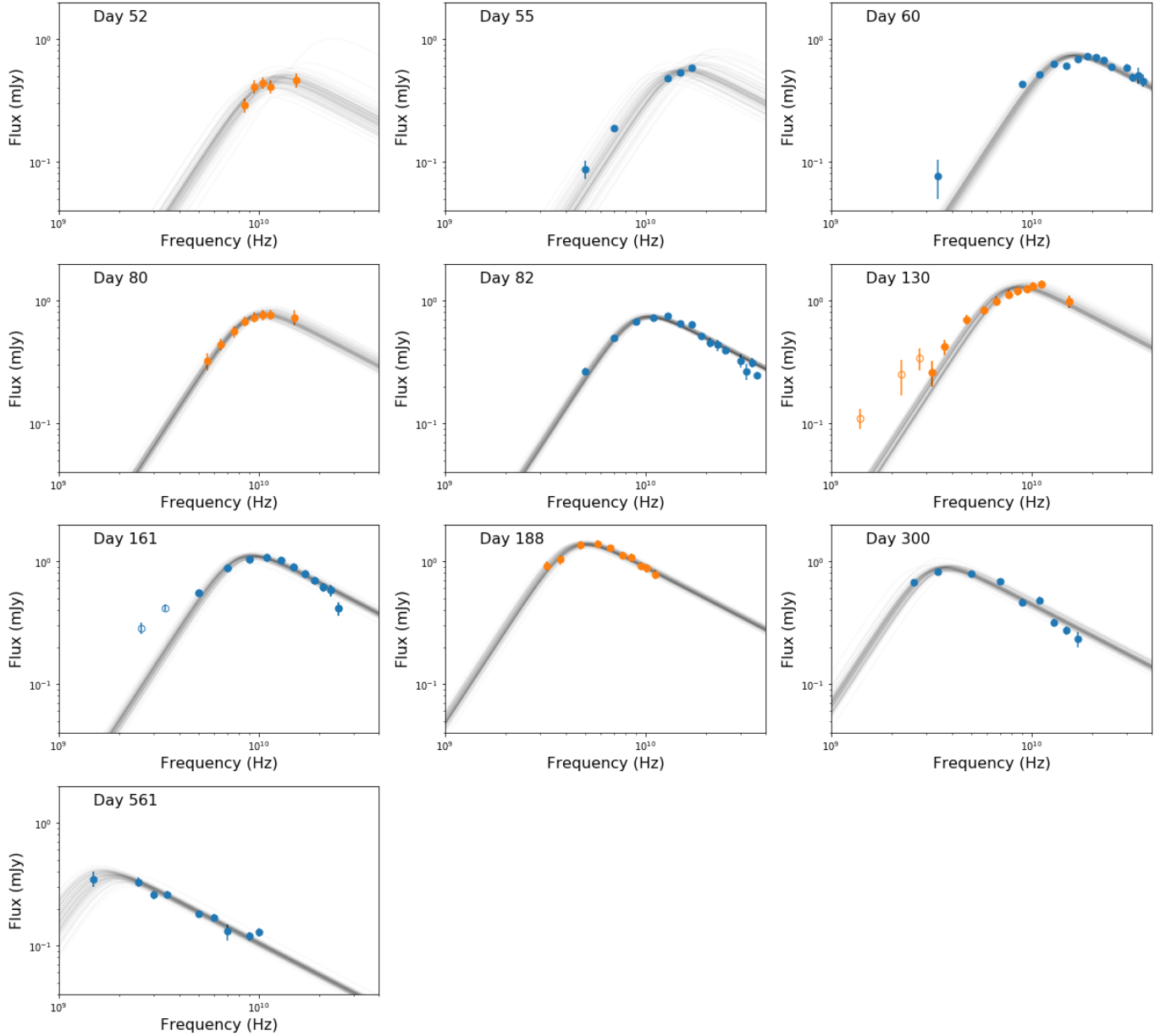


Figure 1. The radio spectral energy distributions for our VLA data (blue), as well as the data in Stein et al. (2021) (orange). The open circles indicate detections that are excluded from the SED fitting. Statistical uncertainties are included in all points but are too small to be visible in most cases. The grey lines are representative fits from our MCMC modeling (§3.1).

include a parameter that accounts for additional systematic uncertainty beyond the statistical uncertainty on the individual data points. The posterior distributions are sampled using 100 MCMC chains, which were run for 2,000 steps, discarding the first 1,000 steps to ensure the samples have sufficiently converged by examining the sampler distribution.

From the SED fits we determine the frequency and flux density of the model SED peak, ν_p and F_p , respectively. The time evolution of these values is shown in Figure 2, where we also include for comparison the val-

ues reported by Stein et al. (2021), although these authors assume $p = 3$ in their analysis. The parameter values are listed in Table 2. In the first two available epochs, 52 days from Stein et al. (2021) and 55 days from our data, we consider ν_p and F_p as essentially lower limits since the SED peak is not well captured by the data. We find that ν_p declines steadily at $\approx 60 - 560$ days as about $t^{-0.85}$. The evolution of F_p is more complex and less typical, with an initial rise by about a factor of 3–4 to about 200 days, and a subsequent decline by about a factor of 4 to 560 days.

Table 2. Spectral Energy Distribution and Equipartition Model Parameters

δt	F_p	$\log(\nu_p)$	$\log(R_{\text{eq}})$	$\log(E_{\text{eq}})$	$\log(B)$	$\log(N_e)$	$\log(n_{\text{ext}})$	$\log(v_{\text{eq}})$
(d)	(mJy)	(Hz)	(cm)	(erg)	(G)		(cm ⁻³)	(m/s)
52 [†] *	0.47 ^{+0.06} _{-0.09}	10.20 ^{+0.10} _{-0.09}	15.92 ^{+0.1} _{-0.05}	47.66 ^{+0.10} _{-0.10}	0.23 ^{+0.14} _{-0.17}	52.35 ^{+0.10} _{-0.10}	3.93 ^{+0.26} _{-0.38}	7.27 ^{+0.10} _{-0.13}
55 [†]	0.60 ^{+0.03} _{-0.04}	10.32 ^{+0.13} _{-0.09}	15.84 ^{+0.09} _{-0.09}	47.66 ^{+0.03} _{-0.03}	0.34 ^{+0.05} _{-0.06}	52.35 ^{+0.03} _{-0.03}	4.15 ^{+0.10} _{-0.12}	7.17 ^{+0.04} _{-0.04}
60	0.67 ^{+0.01} _{-0.01}	10.26 ^{+0.03} _{-0.03}	15.94 ^{+0.03} _{-0.03}	47.78 ^{+0.06} _{-0.03}	0.26 ^{+0.03} _{-0.03}	52.47 ^{+0.03} _{-0.04}	3.99 ^{+0.06} _{-0.06}	7.23 ^{+0.03} _{-0.03}
80*	0.80 ^{+0.06} _{-0.06}	10.14 ^{+0.05} _{-0.06}	16.09 ^{+0.04} _{-0.04}	47.99 ^{+0.05} _{-0.05}	0.14 ^{+0.07} _{-0.05}	52.68 ^{+0.05} _{-0.05}	3.75 ^{+0.13} _{-0.15}	7.25 ^{+0.05} _{-0.06}
82	0.65 ^{+0.03} _{-0.03}	10.03 ^{+0.03} _{-0.03}	16.15 ^{+0.07} _{-0.07}	47.98 ^{+0.09} _{-0.10}	0.05 ^{+0.03} _{-0.07}	52.67 ^{+0.09} _{-0.10}	3.56 ^{+0.12} _{-0.14}	7.30 ^{+0.07} _{-0.07}
130*	1.24 ^{+0.05} _{-0.05}	10.01 ^{+0.04} _{-0.04}	16.30 ^{+0.04} _{-0.04}	48.34 ^{+0.04} _{-0.04}	-0.00 ^{+0.04} _{-0.05}	53.03 ^{+0.04} _{-0.04}	3.46 ^{+0.08} _{-0.09}	7.25 ^{+0.04} _{-0.04}
161	0.98 ^{+0.04} _{-0.04}	9.98 ^{+0.04} _{-0.03}	16.29 ^{+0.07} _{-0.07}	48.25 ^{+0.09} _{-0.10}	-0.03 ^{+0.06} _{-0.07}	52.94 ^{+0.09} _{-0.10}	3.41 ^{+0.12} _{-0.14}	7.15 ^{+0.07} _{-0.07}
188*	1.22 ^{+0.04} _{-0.04}	9.71 ^{+0.04} _{-0.02}	16.60 ^{+0.06} _{-0.06}	48.64 ^{+0.05} _{-0.08}	-0.30 ^{+0.02} _{-0.04}	53.33 ^{+0.07} _{-0.08}	2.86 ^{+0.10} _{-0.11}	7.39 ^{+0.06} _{-0.06}
300	0.79 ^{+0.04} _{-0.04}	9.55 ^{+0.03} _{-0.05}	16.68 ^{+0.1} _{-0.11}	48.58 ^{+0.12} _{-0.14}	-0.45 ^{+0.09} _{-0.09}	53.26 ^{+0.12} _{-0.14}	2.57 ^{+0.17} _{-0.19}	7.27 ^{+0.10} _{-0.11}
561	0.34 ^{+0.03} _{-0.04}	9.23 ^{+0.11} _{-0.11}	16.85 ^{+0.18} _{-0.24}	48.48 ^{+0.23} _{-0.38}	-0.76 ^{+0.14} _{-0.19}	53.17 ^{+0.23} _{-0.038}	1.95 ^{+0.26} _{-0.42}	7.16 ^{+0.18} _{-0.25}

NOTE—Values are assuming $f_A = 1$, $f_V = 0.36$, $\epsilon_e = 0.1$, and $\epsilon_b = 0.02$.

* Flux density measurements obtained from Stein et al. (2021).

† Parameters derived from these observations are excluded from our analysis, but included here for completeness (see text).

3.2. Equipartition Analysis

Using the inferred values of ν_p and F_p from §3.1, we can now derive the physical properties of the outflow using an equipartition analysis. We focus on the case of a non-relativistic spherical outflow using the following expressions for the radius and kinetic energy (see Equations 27 and 28 in Barniol Duran et al. 2013), with $p = 2.7$:

$$R_{\text{eq}} \approx (9.1 \times 10^{22} \text{ cm}) \times F_{p,\text{mJy}}^{8.7/18.4} d_{L,28}^{17.4/18.4} \nu_{p,10}^{-1} \\ \times (1+z)^{-27.1/18.4} f_A^{-7.7/18.4} f_V^{-1/18.4} 4^{1/18.4} \epsilon^{1/17} \\ \times \xi^{1/18.4} \gamma_m^{-0.7/18.4} \quad (2)$$

$$E_{\text{eq}} \approx (2.17 \times 10^{50} \text{ erg}) \times F_{p,\text{mJy}}^{22.1/18.4} d_{L,28}^{44.2/18.4} \nu_{p,10}^{-1} \\ \times (1+z)^{-40.5/18.4} f_A^{-11.1/18.4} f_V^{7.4/18.4} 4^{11/18.4} \xi^{11/18.4} \\ \times \gamma_m^{0.75} [(11/17)\epsilon^{-6/17} + (6/17)\epsilon^{11/17}], \quad (3)$$

where $d_L \approx 230$ Mpc is the luminosity distance; $z = 0.051$ is the redshift; $f_A = 1$ and $f_V = \frac{4}{3} \times (1 - 0.9^3) = 0.36$ are the area and volume filling factors, respectively, where we assume that the emitting region is a shell of thickness $0.1R_{\text{eq}}$; and $\gamma_m = 2$ is the minimum Lorentz factor as relevant for non-relativistic sources (Barniol Duran et al. 2013). We chose these factors for f_A and f_V since there is no evidence for significant beaming (see §4.2), and thus the simplest assumption is a roughly spherical outflow. The factors of $4^{1/18.4}$ and $4^{11/18.4}$ for the radius and energy, respectively, arise

from corrections to the isotropic number of radiating electrons ($N_{e,\text{iso}}$) in the non-relativistic case. We further assume that the fraction of post-shock energy in relativistic electrons is $\epsilon_e = 0.1$, which leads to correction factors of $\xi^{1/18.4}$ and $\xi^{11/18.4}$ in R_{eq} and E_{eq} , respectively, with $\xi = 1 + \epsilon_e^{-1} \approx 11$. Finally, we parameterize any deviation from equipartition with a correction factor $\epsilon = (11/6)(\epsilon_B/\epsilon_e)$, where ϵ_B is the fraction of post-shock energy in magnetic fields.

The magnetic field strength and the number of radiating electrons are given by (see Equations 16 and 15 in Barniol Duran et al. 2013):

$$B \approx (1.3 \times 10^{-2} \text{ G}) \times F_{p,\text{mJy}}^{-2} d_{L,28}^{-4} (1+z)^7 f_A^2 R_{\text{eq},17}^4 \nu_{p,10}^5 \quad (4)$$

$$N_e \approx (4 \times 10^{54}) \times F_{p,\text{mJy}}^3 d_{L,28}^6 (1+z)^{-8} f_A^{-2} R_{\text{eq},17}^{-4} \nu_{p,10}^{-5} \\ \times (\gamma_a/\gamma_m)^{(p-1)}, \quad (5)$$

where the Lorentz factor of electrons that radiate at ν_a is given by:

$$\gamma_a \approx 525 \times F_{p,\text{mJy}} d_{L,28}^2 \nu_{p,10}^{-2} (1+z)^{-3} f_A^{-1} R_{\text{eq},17}^{-2}, \quad (6)$$

We will note explicitly that the extra factor of 4 and extra correction factor $(\gamma_a/\gamma_m)^{(p-1)}$ are added correction factors for the Newtonian regime (Duran, private communication). We calculate the density of the ambient medium as $n_{\text{ext}} = N_e/4V$, where V is the volume of the emission region assumed to be a spherical shell of thickness $0.1R_{\text{eq}}$ and the factor of $\frac{1}{4}$ is due to the shock jump conditions.

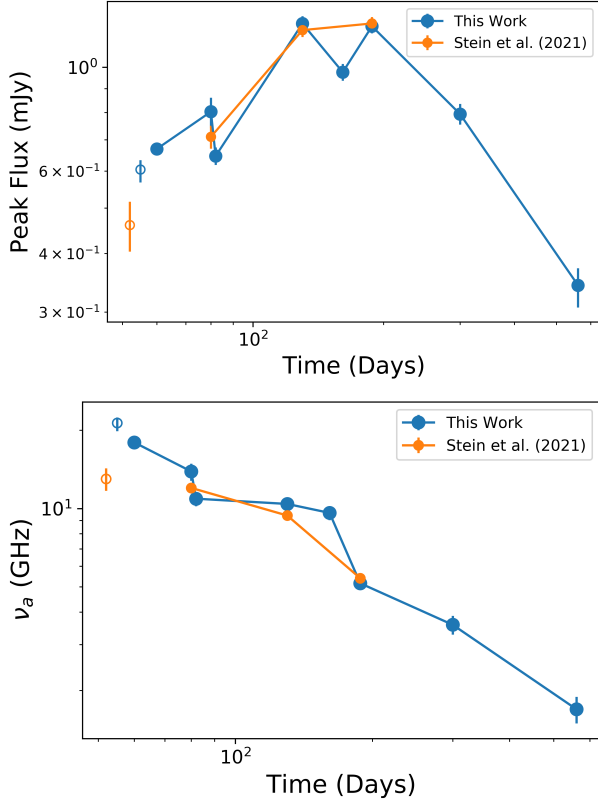


Figure 2. Time evolution of the synchrotron peak flux density (*Left*) and peak frequency (*Right*) from the SED modeling of the data in Figure 1. The blue points indicate our fits to the entire data set (including the data from Stein et al. 2021), while the orange points are taken from the analysis of Stein et al. (2021). Open circles represent epochs in which the values should be taken as lower limits due to the lack of data above the peak frequency. These points are not used in the subsequent analysis.

3.3. Cooling Frequency and ϵ_B

Our ALMA observations allow us to investigate the presence of a cooling break between the VLA and ALMA bands. The synchrotron cooling frequency is given by (Sari et al. 1998):

$$\nu_c = 2.8 \times 10^6 \gamma_c^2 B, \quad (7)$$

where $\gamma_c = 6\pi m_e c / \sigma_T B^2 t$, with t being the age of the system.

In Figure 3 we show our VLA+ALMA SEDs at 82–84 and 161–188 days, along with our model SED from §3.1, which does not include a cooling break (grey lines). This model clearly over-predicts the ALMA measurements (and already begins to deviate from the data at ≈ 25 –30 GHz). The steepening required by the ALMA data is indicative of a cooling break, which we model with an additional multiplicative term to Equation 1 (Granot &

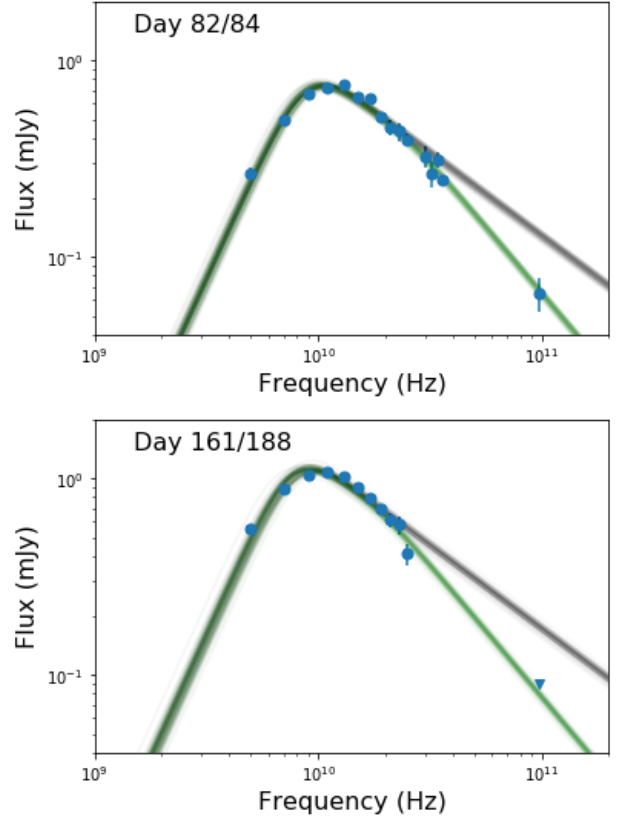


Figure 3. VLA + ALMA data (blue) at 82–84 days (*Top*) and 161–188 days (*Bottom*), where circles are detections and the ALMA upper limit is marked with a triangle. Also shown are the models from Figure 1 (grey; no cooling break), and models that include a synchrotron cooling break (green; Equation 8). At 82–84 days we find that $\nu_c \approx 25$ GHz, leading to $\epsilon_B \approx 0.02$ (§3.3). At 161–188 days, we find that $\nu_c \approx 20$ GHz, leading to a consistent value of $\epsilon_B \approx 0.01$.

Sari 2002):

$$\left[1 + \left(\frac{\nu}{\nu_c} \right)^{s_3(\beta_3 - \beta_4)} \right]^{-1/s_3}, \quad (8)$$

where $\beta_4 = -p/2$ and we use $s_3 = 10$.⁵

For our observation at 82–84 days we find that $\nu_c \approx 25$ GHz provides a much better fit to the high frequency data (Figure 3). With the value of ν_c determined, we adjust the value of ϵ_B and solve Equation 7 after repeating the equipartition analysis (Equations 2

⁵ We note that our choice for s_3 is steeper than the value in Granot & Sari (2002), and is motivated by the actual observed sharpness in the break and by the fact that Granot & Sari (2002) formalism has been derived in the context of relativistic events (specifically, GRB afterglows). With potential future detections of cooling breaks in TDEs we may be able to assess whether the shape of the break is similar to this event, or more in line with the Granot & Sari (2002) theoretical formalism.

to 5) to account for the deviation from equipartition in those parameters. Specifically, we find that with the inclusion of a cooling frequency, $\epsilon_B \ll 0.1$ in order for these equations to remain consistent, otherwise ν_c is significantly higher than what our data indicates. With this approach, we find $\epsilon_B \approx 0.02$. For our observations at 161–188 days, we find that $\nu_c \approx 20$ GHz best fits our data, indicating a consistent value of $\epsilon_B \approx 0.01$. Since the observation covering 82–84 days includes a detection, we adopt $\epsilon_B \approx 0.02$ in our analysis. Moreover, using the time evolution of the relevant parameters we find that the time evolution of ν_c does not violate the non-detection of a break in the other SEDs, which are in any case mainly restricted to $\lesssim 30$ GHz.

3.4. Outflow and Ambient Medium Properties

The inferred outflow parameters as a function of time, as well as the circumnuclear density as a function of radius, are plotted in Figure 4. The calculated parameters are also listed in Table 2. We find that the radius increases steadily as a power law with $R \propto t^{0.9}$, with a value of about 10^{16} cm at 60 days. This is roughly consistent with free expansion, and we infer a mean velocity of $v \approx 0.07c$ at 60–560 days, justifying our assumption in §3.2 of non-relativistic expansion. The kinetic energy exhibits an increase by about a factor of 5 at 60–200 days ($E_K \propto t^{1.5}$), and then plateaus at a value of $E_K \approx 4 \times 10^{48}$ erg. We additionally find a steady decline in the magnetic field strength, with $B \propto t^{-1.0}$ (or $B \propto R^{-1.1}$), and a value of about 1.8 G at 60 days. The circumnuclear density evolves as $n_{\text{ext}} \propto t^{-2.0}$, or equivalently on average as $\propto R^{-2.1}$. Plotting n_{ext} as a function of R , we find a possibly more complex structure, with a profile of $n_{\text{ext}} \propto R^{-1.7}$ at $\approx (1-4) \times 10^{16}$ cm, and a steeper $n_{\text{ext}} \propto R^{-3.9}$ to $\approx 7 \times 10^{16}$ cm.

The trends in our data are also evident in the more restricted time range of the analysis in Stein et al. (2021) when compared to their equipartition values. We find systematic offsets in E_K (their values lower by a factor of 1.5), B (lower by a factor of 1.3), and n_{ext} (higher by a factor of 1.4); see Figure 4. The offsets are due to a combination of a different choice of p (2.7 in our analysis versus 3 in theirs) and our determination of $\epsilon_B \approx 0.02$ based on the detection of a cooling break.

4. AT2019dsg IN THE CONTEXT OF OTHER TDES

4.1. Outflow Velocity and Kinetic Energy

We find that the radio emission from AT2019dsg is due to a non-relativistic outflow with $v \approx 0.07c$ and a kinetic energy that rises as $E_K \propto t^{1.5}$ at 60–200 days to a plateau at 4×10^{48} erg. The rise in energy could be

due to a sustained injection of energy from the central engine (accreting SMBH), or to a rapid initial ejection but with a spread of velocities. The latter effect is apparent in Type Ib/c SNe and in some long GRBs (Laskar et al. 2014, 2015; Margutti et al. 2014; Bietenholz et al. 2021). In the case of AT2019dsg since the velocity is roughly constant the more likely explanation for the increase in energy is continued injection due to sustained accretion onto the SMBH. A more detailed exploration of this effect will benefit from a detailed analysis of the optical/UV data and an inference of the mass accretion rate as a function of time; this is beyond the scope of this paper.

In Figure 5 we place the outflow from AT2019dsg in the context of other radio-emitting TDEs, as well as long GRBs and Type Ib/c SNe. We find that the outflow in AT2019dsg clusters with those of previous TDEs with $E_K \approx 10^{48} - 10^{49}$ erg and $v \sim 0.1c$. It is clearly distinguished from the relativistic TDE Sw J1644+57 with $\Gamma \sim \text{few}$ and $E_K \sim 10^{52}$ erg (Zauderer et al. 2011; Berger et al. 2012). However, we note that like AT2019dsg, Sw J1644+57 also exhibited an order of magnitude increase in its energy at early times (Berger et al. 2012), and to date these TDEs are the only two with multi-frequency radio detections covering the early period post-disruption ($t_d \lesssim 100$ days).

We also find that the outflow energy and velocity of AT2019dsg (and the other non-relativistic TDEs) are comparable to those seen in radio-emitting Type Ib/c SNe (Figure 5). Stein et al. (2021) report a neutrino event discovered on 2019 October 1, which they associate with AT2019dsg based on a rough spatial coincidence, and despite the several months delay between the disruption and the neutrino event. A variety of emission mechanisms have been proposed for this neutrino, but many of those that depend on the presence of a jet or outflow in AT2019dsg require a larger outflow energy than we find in our analysis (Fang et al. 2020; Winter & Lunardini 2020; Liu et al. 2020; Murase et al. 2020). The ordinary outflow properties of AT2019dsg in the context of TDEs and Type Ib/c SNe weakens the argument for such an association, as neutrinos have not previously been associated with these events, and Type Ib/c SNe are much more common than TDEs.

4.2. Relativistic Outflow

In our analysis we assume that the outflow from AT2019dsg is isotropic, which is consistent with the inference of a non-relativistic outflow. If we instead assume that the outflow is collimated, then the inferred radius (and hence the velocity) will increase. Here we consider what outflow collimation is required to result

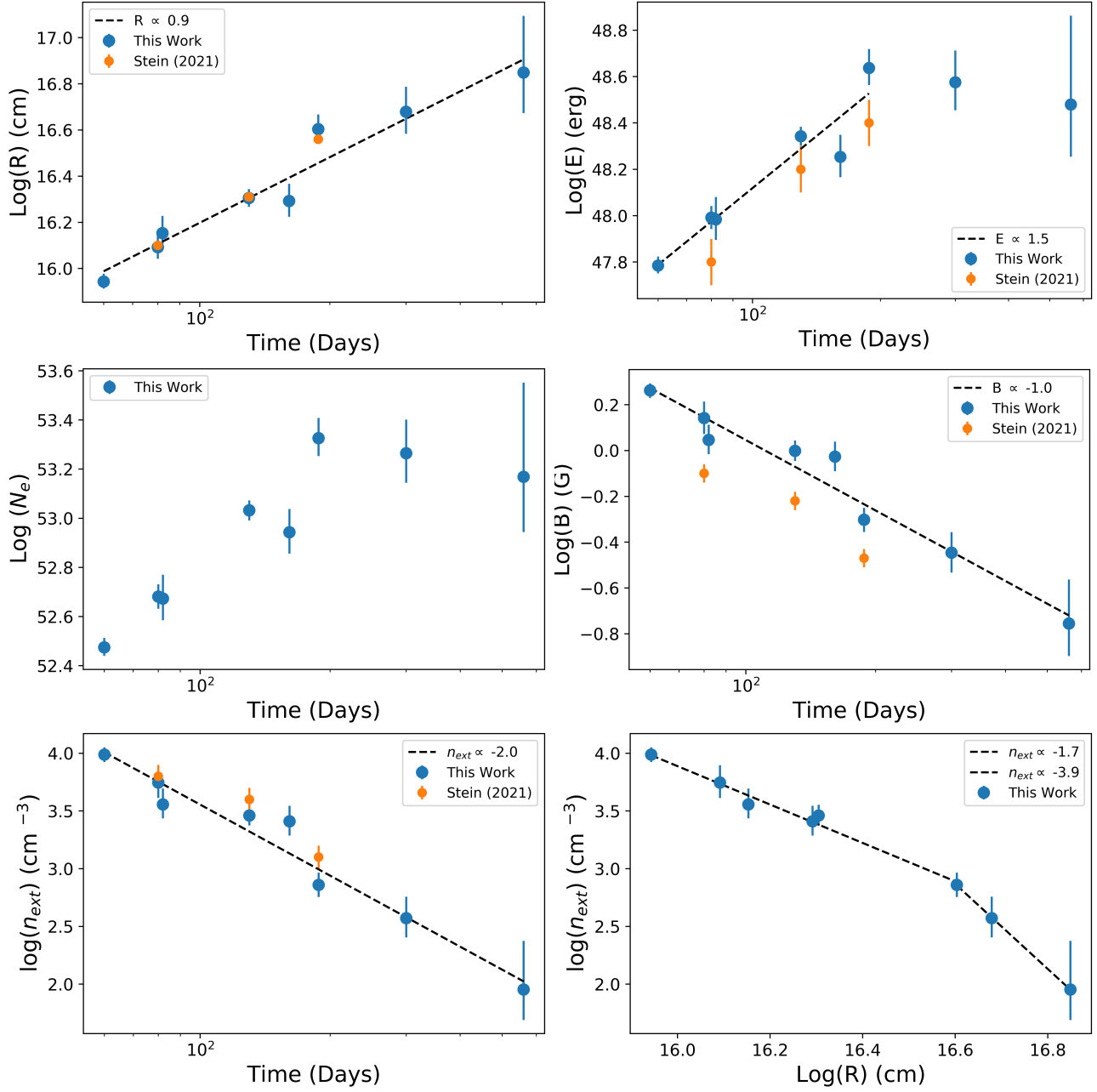


Figure 4. Time evolution of the outflow and density parameters: R , E_K , N_e , B , and n_{ext} , as well as the radial profile of n_{ext} (bottom right panel). The blue points mark the results of our analysis of the entire data set (including the data from Stein et al. 2021), while the orange points are taken from the analysis of Stein et al. (2021) when assuming a spherical outflow with no deviation from equipartition present. The dashed lines are power law fits to the data, with the inferred index given in each panel.

in a mildly relativistic outflow, with $\Gamma = 2$. This corresponds to the “narrow jets” solution in Barniol Duran et al. (2013), with $f_A = f_V = (\theta_j \Gamma)^2$, for a collimated jet with a half-opening angle θ_j . Applying these geometric factors in Equation 2, we find a self-consistent solution for $\theta_j \approx 0.035$ rad (2°), narrow even in the context of GRBs (Frail et al. 2001). To produce a truly relativistic outflow ($\Gamma \sim 10$) would require an unphysical outflow

with $\theta_j \ll 1^\circ$. Therefore, our conclusion that the outflow in AT 2019dsg is non-relativistic is robust.

4.3. Circumnuclear Density

In Figure 6 we compare the inferred circumnuclear density profile surrounding AT 2019dsg with those around previous radio-emitting TDEs, as well as to the environments of Sgr A* and M87*. In all cases we scale

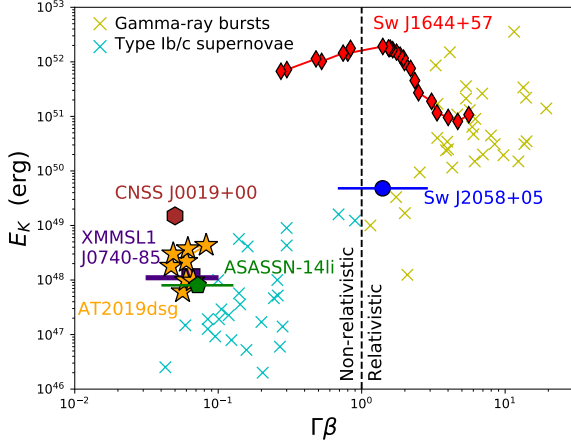


Figure 5. The energy/velocity of various TDEs including AT2019dsg. AT2019dsg’s radio emission shows similar energetics to other transients known to launch non-relativistic outflows, including TDEs (Alexander et al. 2016, 2017; Anderson et al. 2019) and Type Ib/c supernovae (SNe; sample from Margutti et al. 2014). In both the TDE and SN populations, only a small fraction of events launch energetic relativistic jets (Cenko et al. 2012; Margutti et al. 2014; Zauderer et al. 2011; Cendes et al. 2021), suggesting that the conditions required for the formation of such jets are rare.

the radial profile by the relevant SMBH’s Schwarzschild radius. For AT2019dsg we use the value of $\log M_{\text{SMBH}} = 6.7 \pm 0.4 M_{\odot}$, or $R_s = (1.6 \pm 0.9) \times 10^{12}$ cm (Cannizzaro et al. 2020). With this value, our observations span a scale of $\approx (5-44) \times 10^3 R_s$. The density profile is similar to that inferred in ASASSN-14li (Alexander et al. 2016). The inner portion of the sampled profile, $\rho \propto R^{-1.7}$, is roughly consistent with expectations for spherical Bondi accretion, while the final three epochs show evidence for a steepening.

5. CONCLUSIONS

We presented detailed VLA and ALMA observations of the TDE AT2019dsg, spanning 55 to 560 days after disruption. Using these data we inferred the physical properties of the outflow and the circumnuclear environment. We find that the outflow is non-relativistic ($v \approx 0.07c$) with a total kinetic energy of $\approx 4 \times 10^{48}$ erg, typical of previous non-relativistic TDEs. The energy exhibits an initial rise as $E_K \propto t^{1.5}$ to about 200 days, which is likely indicative of continuous energy injection. The circumnuclear medium has a density of about $1 \times 10^4 \text{ cm}^{-3}$ at a radius of 10^{16} cm ($6 \times 10^3 R_s$) and follows a steep radial decline of about $R^{-1.7}$ with a potential further steepening at about $2.5 \times 10^4 R_s$.

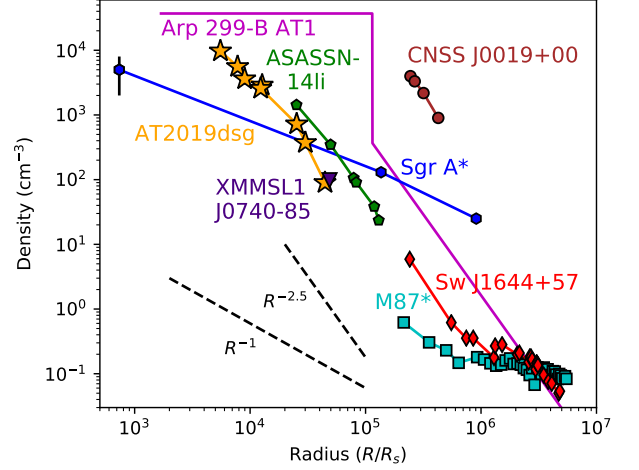


Figure 6. The circumnuclear density profile derived from various TDEs including AT2019dsg, normalized to the Schwarzschild radius of the SMBH at each host galaxy’s center. AT2019dsg’s host galaxy has a steep density profile, similar to those seen in other non-relativistic TDEs (e.g. ASASSN-14li, Alexander et al. 2016, and CNSS J0019+00, Anderson et al. 2019). We also show the density profiles calculated for several other TDEs (Alexander et al. 2017; Mattila et al. 2018; Eftekhari et al. 2018) and for the Milky Way (Baganoff et al. 2003; Gillessen et al. 2019) and M87 (Russell et al. 2015).

We further find that a mildly relativistic outflow would require an unexpectedly narrow opening angle of $\theta_j \approx 2^\circ$, while a truly relativistic outflow is unphysical. The ordinary nature of the outflow in AT2019dsg relative to other TDEs and to Type Ib/c SNe (which are more common) casts doubt on the claimed association of this event with a high-energy neutrino.

Software: CASA (McMullin et al. 2007), pwkit (Williams et al. 2017)

ACKNOWLEDGMENTS

We thank Joe Lazio with his assistance with the NE2001 model. The Berger Time-Domain Group at Harvard is supported by NSF and NASA grants. K.D.A. is supported by NASA through the NASA Hubble Fellowship grant #HST-HF2-51403.001-A awarded by the Space Telescope Science Institute, which is operated by the Association of Universities for Research in Astronomy, Inc., for NASA, under contract NAS5-26555. This paper makes use of the following ALMA data: ADS/JAO.ALMA#2018.1.01766.T. ALMA is a partnership of ESO (representing its member states), NSF (USA) and NINS (Japan), together with NRC (Canada), MOST and ASIAA (Taiwan), and KASI (Republic of Korea), in cooperation with the Republic of Chile. The Joint ALMA Observatory is operated by ESO, AUI/NRAO and NAOJ. The National Radio Astronomy Observatory is a facility of the National Science Foundation operated under cooperative agreement by Associated Universities, Inc.

APPENDIX

A. INTERSTELLAR SCINTILLATION

In the observations at days 130 and 161 we find excess emission at about 1.5 – 3 GHz. Here we consider if these are consistent with interstellar scintillation (Goodman 1997), which is known to affect low frequency radio emission from compact sources. Using the Galactic coordinates of AT 2019dsg in the NE2001 electron density model (Cordes & Lazio 2002), we find a scattering measure of $SM \approx 0.34 \times 10^{-3} \text{ kpc-m}^{-20/3}$, and a transition frequency $\nu_{ss} \approx 14 \text{ GHz}$. Combining these parameters, we find a scattering screen distance of $d_{scr} \approx 5.64\nu_{ss}^{-1}(SM_{-3.5})^{6/5} \approx 2.5 \text{ kpc}$. The critical radius for diffractive scintillation, which can result in order unity flux variations, is $\theta_{crit} \approx 2.35(SM_{-3.5})^{-3/17}d_{scr,kpc}^{-11/17} \approx 1.3 \mu\text{as}$. For AT 2019dsg we infer an angular radius of 3.2 μas at 60 days (and 20 μas at 560 days), indicating that diffractive scintillation is not expected. On the other hand, refractive scintillation is relevant on this size scale. Following Goodman (1997) we expect the peak frequency for refractive scintillation to be $\sim 4 \text{ GHz}$ with a modulation index of ~ 0.3 , which is consistent with the observed flux variations.

REFERENCES

- Alexander, K. D., Berger, E., Guillochon, J., Zauderer, B. A., & Williams, P. K. G. 2016, *ApJL*, 819, L25, doi: [10.3847/2041-8205/819/2/L25](https://doi.org/10.3847/2041-8205/819/2/L25)
- Alexander, K. D., van Velzen, S., Horesh, A., & Zauderer, B. A. 2020, arXiv e-prints, arXiv:2006.01159, <https://arxiv.org/abs/2006.01159>
- Alexander, K. D., Wieringa, M. H., Berger, E., Saxton, R. D., & Komossa, S. 2017, *ApJ*, 837, 153, doi: [10.3847/1538-4357/aa6192](https://doi.org/10.3847/1538-4357/aa6192)
- Anderson, M. M., Mooley, K. P., Hallinan, G., et al. 2019, arXiv e-prints, arXiv:1910.11912, <https://arxiv.org/abs/1910.11912>
- Baganoff, F. K., Maeda, Y., Morris, M., et al. 2003, *ApJ*, 591, 891, doi: [10.1086/375145](https://doi.org/10.1086/375145)
- Barniol Duran, R., Nakar, E., & Piran, T. 2013, *ApJ*, 772, 78, doi: [10.1088/0004-637X/772/1/78](https://doi.org/10.1088/0004-637X/772/1/78)
- Berger, E., Zauderer, A., Pooley, G. G., et al. 2012, *ApJ*, 748, 36, doi: [10.1088/0004-637X/748/1/36](https://doi.org/10.1088/0004-637X/748/1/36)
- Bietenholz, M. F., Bartel, N., Argo, M., et al. 2021, *ApJ*, 908, 75, doi: [10.3847/1538-4357/abccd9](https://doi.org/10.3847/1538-4357/abccd9)
- Cannizzaro, G., Wevers, T., Jonker, P. G., et al. 2020, arXiv e-prints, arXiv:2012.10195, <https://arxiv.org/abs/2012.10195>

- Cendes, Y., Eftekhari, T., Berger, E., & Polisensky, E. 2021, *ApJ*, 908, 125, doi: [10.3847/1538-4357/abd323](https://doi.org/10.3847/1538-4357/abd323)
- Cenko, S. B., Krimm, H. A., Horesh, A., et al. 2012, *ApJ*, 753, 77, doi: [10.1088/0004-637X/753/1/77](https://doi.org/10.1088/0004-637X/753/1/77)
- Cordes, J. M., & Lazio, T. J. W. 2002, arXiv e-prints, astro. <https://arxiv.org/abs/astro-ph/0207156>
- Eftekhari, T., Berger, E., Zauderer, B. A., Margutti, R., & Alexander, K. D. 2018, *ApJ*, 854, 86, doi: [10.3847/1538-4357/aaa8e0](https://doi.org/10.3847/1538-4357/aaa8e0)
- Fang, K., Metzger, B. D., Vurm, I., Aydi, E., & Chomiuk, L. 2020, *ApJ*, 904, 4, doi: [10.3847/1538-4357/abbc6e](https://doi.org/10.3847/1538-4357/abbc6e)
- Foreman-Mackey, D., Hogg, D. W., Lang, D., & Goodman, J. 2013, *PASP*, 125, 306, doi: [10.1086/670067](https://doi.org/10.1086/670067)
- Frail, D. A., Kulkarni, S. R., Sari, R., et al. 2001, *ApJL*, 562, L55, doi: [10.1086/338119](https://doi.org/10.1086/338119)
- Gillessen, S., Plewa, P. M., Widmann, F., et al. 2019, *ApJ*, 871, 126, doi: [10.3847/1538-4357/aaf4f8](https://doi.org/10.3847/1538-4357/aaf4f8)
- Goodman, J. 1997, *NewA*, 2, 449, doi: [10.1016/S1384-1076\(97\)00031-6](https://doi.org/10.1016/S1384-1076(97)00031-6)
- Granot, J., & Sari, R. 2002, *ApJ*, 568, 820, doi: [10.1086/338966](https://doi.org/10.1086/338966)
- Laskar, T., Berger, E., Margutti, R., et al. 2015, *ApJ*, 814, 1, doi: [10.1088/0004-637X/814/1/1](https://doi.org/10.1088/0004-637X/814/1/1)
- Laskar, T., Berger, E., Tanvir, N., et al. 2014, *ApJ*, 781, 1, doi: [10.1088/0004-637X/781/1/1](https://doi.org/10.1088/0004-637X/781/1/1)
- Lee, C.-H., Hung, T., Matheson, T., et al. 2020, *ApJL*, 892, L1, doi: [10.3847/2041-8213/ab7cd3](https://doi.org/10.3847/2041-8213/ab7cd3)
- Liu, R.-Y., Xi, S.-Q., & Wang, X.-Y. 2020, *PhRvD*, 102, 083028, doi: [10.1103/PhysRevD.102.083028](https://doi.org/10.1103/PhysRevD.102.083028)
- Margutti, R., Milisavljevic, D., Soderberg, A. M., et al. 2014, *ApJ*, 797, 107, doi: [10.1088/0004-637X/797/2/107](https://doi.org/10.1088/0004-637X/797/2/107)
- Mattila, S., Pérez-Torres, M., Efstathiou, A., et al. 2018, *Science*, 361, 482, doi: [10.1126/science.aao4669](https://doi.org/10.1126/science.aao4669)
- McMullin, J. P., Waters, B., Schiebel, D., Young, W., & Golap, K. 2007, in *Astronomical Society of the Pacific Conference Series*, Vol. 376, *Astronomical Data Analysis Software and Systems XVI*, ed. R. A. Shaw, F. Hill, & D. J. Bell, 127
- Murase, K., Kimura, S. S., Zhang, B. T., Oikonomou, F., & Petropoulou, M. 2020, *ApJ*, 902, 108, doi: [10.3847/1538-4357/abb3c0](https://doi.org/10.3847/1538-4357/abb3c0)
- Russell, H. R., Fabian, A. C., McNamara, B. R., & Broderick, A. E. 2015, *MNRAS*, 451, 588, doi: [10.1093/mnras/stv954](https://doi.org/10.1093/mnras/stv954)
- Sari, R., Piran, T., & Narayan, R. 1998, *ApJL*, 497, L17, doi: [10.1086/311269](https://doi.org/10.1086/311269)
- Stein, R., Velzen, S. v., Kowalski, M., et al. 2021, *Nature Astronomy*, doi: [10.1038/s41550-020-01295-8](https://doi.org/10.1038/s41550-020-01295-8)
- van Velzen, S., Gezari, S., Hammerstein, E., et al. 2020, arXiv e-prints, arXiv:2001.01409. <https://arxiv.org/abs/2001.01409>
- Williams, P. K. G., Gizis, J. E., & Berger, E. 2017, *ApJ*, 834, 117, doi: [10.3847/1538-4357/834/2/117](https://doi.org/10.3847/1538-4357/834/2/117)
- Winter, W., & Lunardini, C. 2020, arXiv e-prints, arXiv:2005.06097. <https://arxiv.org/abs/2005.06097>
- Zauderer, B. A., Berger, E., Soderberg, A. M., et al. 2011, *Nature*, 476, 425, doi: [10.1038/nature10366](https://doi.org/10.1038/nature10366)